INTERNATIONAL JOURNAL FOR NUMERICAL METHODS IN FLUIDS
Int. J. Numer. Meth. Fluids 2007; **53**:1629–1646
Published online 10 October 2006 in Wiley InterScience (www.interscience.wiley.com). DOI: 10.1002/fld.1376

Numerical simulation of the galvanizing process during GA to GI transition

F. Ilinca[1,*,†], F. Ajersch[2,‡], C. Baril[3,§] and F. E. Goodwin[4,¶]

[1]*National Research Council, 75 de Mortagne, Boucherville, Que., Canada J4B 6Y4*
[2]*École Polytechnique de Montréal, Montréal, Que., Canada H3C 3A7*
[3]*Sorevco Inc., Coteau-du-Lac, Qué., Canada J0P 1B0*
[4]*International Lead Zinc Research Organization, 2525 Meridian Parkway, Research Triangle Park, NC 27709-2036, U.S.A.*

SUMMARY

This paper presents the application of a three-dimensional finite element solution algorithm for the prediction of the velocity, temperature and species concentration fields in an industrial continuous galvanizing bath. Simulations were carried out using a parallel CFD software developed at IMI-NRC. The turbulent flow, heat and mass transfer has been solved using a high Reynolds number k–ε model. Simulations were carried out for the case when the density of the molten metal depends only on the temperature and also for the case when both temperature and Al concentration affect the density. When considering the buoyancy effect of the Al concentration, differences are especially apparent during the melting of ingots with high Al content. Otherwise, thermal effects are dominant. The continuous monitoring of the temperature and the Al and Fe content in an industrial bath was used to validate the flow, temperature and compositional variations. A period of three hours, corresponding to three different ingot additions, was simulated successfully, resulting in a good agreement of the temperature and compositional variations.

Received 16 June 2006; Revised 11 August 2006; Accepted 16 August 2006

KEY WORDS: galvanizing bath; Al and Fe content; 3D transient flow; finite elements; experimental validation

*Correspondence to: F. Ilinca, National Research Council, Industrial Materials Institute, 75 de Mortagne, Boucherville, Qué., Canada J4B 6Y4.
†E-mail: florin.ilinca@cnrc-nrc.gc.ca
‡E-mail: frank.ajersch@polymtl.ca
§E-mail: cbaril@sorevco.com
¶E-mail: fgoodwin@ilzro.org

Contract/grant sponsor: International Lead Zinc Research Organization

1. INTRODUCTION

The hot dip galvanizing process is a complex metallurgical process where steel strip of various width and thickness is continuously coated by rapid immersion in a zinc alloy bath normally between 450 and 480°C (see Figure 1). On exiting from the bath, the excess zinc solution is deflected back into the bath by means of air knives, leaving a thin coating on the steel sheet. Aluminium presence in the galvanizing bath is essential in order to obtain an adherent coating with good formability. Concentration levels for the galvanneal (GA) product are in the range from 0.11 to 0.13% Al and up to 0.20% Al for the galvanized (GI) product. The rapid reaction of the aluminium in the bath with steel forms an inhibition layer of Fe_2Al_5 generally less than 1 μm thick which is both adherent and deformable as opposed to the iron zinc intermetallics which are much more fragile. On exiting the bath this solid layer is covered with an entrained liquid layer of the alloy at the bath composition. The air knives at the exit of the strip control the coating thickness by variation of air pressure and gap width from the strip. The material consumption is compensated by the ingots which are added to the bath. Make up ingots of zinc alloy have usually between 0.5 and 1.0 wt% Al depending on the type of product or operation. Local decreases in the temperature near the melting ingot surface reduce the solubility of both iron and aluminium, and are considered to be the primary source of dross particles (precipitates of Fe_2Al_5) which can nucleate and grow. Control of bath temperature is therefore of primary importance in order to prevent this precipitation phenomena. Dross formation is considered to be the major difficulty to overcome in the production of high quality coatings. Since the production of high quality zinc coated products is a major factor in the profitability of all steel sheet producers, the technology and quality control of the galvanizing process is of primary concern [1]. Numerical modelling can play an important role in improving the understanding of the process in order to reach an optimum setting of the parameters.

Numerical solutions of the flow regime in a continuous zinc galvanizing bath have been carried out over a number of years in projects sponsored by the International Lead Zinc Research Organization [2, 3] as well as in other studies [4, 5]. With the development of more sophisticated computational techniques and high speed processors, the numerical models can now handle very

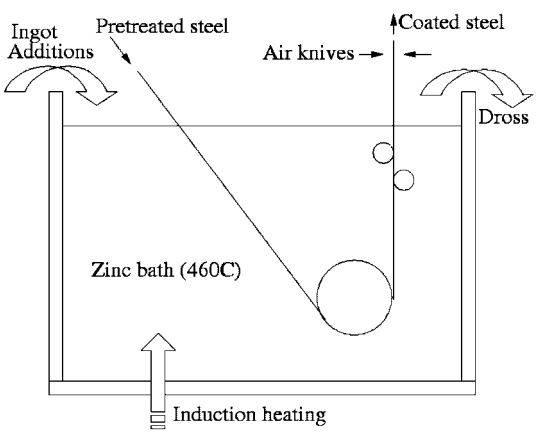

Figure 1. Schema of a galvanizing bath operation.

DOI: 10.1002/fld

complex flow systems with a large number of grid points resulting in a detailed prediction of flow. The authors have previously shown the importance of the temperature variations on the flow as compared to the isothermal case [6–8]. Heat losses through the pot sidewalls, bottom, and bath surface were taken into account in the heat balance. The effect of changing line speed, strip width, strip temperature and inductor power was also quantified. During the ingot melting period the induction heating rate is increased to compensate for the heat demand of the melting ingot, thereby increasing temperature variations in the bath. The temperature at the inductor exit is higher and the region at the melting surface of the ingot is lower than the average bath temperature. It has been shown that temperature variations in the bath affect the overall flow due to natural convection, especially in regions where forced convection is small. This occurs in regions away from the moving strip and the immersion rollers, in regions that are significantly affected by the temperature variations during ingot melting. Solution of the thermal field is also important because intermetallic particles of dross form when the temperature in the zinc bath falls below the solubility limit of the solute components of aluminium and iron in liquid zinc [9, 10].

An experimental validation of the 3D solution algorithm using a water bath model was reported by Ouellet *et al.* [11]. Numerical simulations of the flow, the temperature variations, and the distribution of Al and Fe in a typical galvanizing bath have previously been carried out successfully by the authors [12, 13]. The modelling of the Al and Fe distribution in the bath in these studies assumes that the Zn solution will always tend to reach the solubility limits of Al and Fe as determined by the phase diagram [14]. Local variations in the solubility of these elements are the result of temperature variations that occur during ingot melting, and from the heat input required to maintain the overall thermal balance. In carrying out the numerical simulations of the composition variations, it was assumed that the solubility limits were reached instantaneously, and that any new addition of Al results in the nucleation of either top dross (Fe_2Al_5) or bottom dross ($FeZn_7$ or $FeZn_{13}$) particles when the total Al or Fe exceeds the solubility limit of the specific composition of the bath. Also, these particles were assumed to be of sufficiently small size such that they would be transported with the Zn flow without settling or floating, and that no agglomeration of these particles would occur during their movement within the bath. The simulations, based on these assumptions, have successfully demonstrated the sensitivity of dross formation to temperature variations.

The galvanizing bath configuration of this study is shown in Figure 2. We can see the sink and stabilization rolls, the roll arms, the snout and the moving strip. The snout has the role of protecting the strip at the entry in the bath. The present configuration represents a bath of 75 ton of zinc and 1 ton ingots are added at approximately 1 h interval. The LIBS probe [15] and the Teck Cominco setup [16] are located on one side and ingots are charged on the other side of the pot. Calibration of the instrumental results was carried out on compositions of standard samples. In addition to in-line measurements, bath samples taken during the test period were analysed by Sorevco using Atomic Absorption and by Canadian Electrolytic Zinc (CEZ) using ICP.

The purpose of the present paper is to advance the understanding of flow in the galvanizing bath particularly during the galvanneal (GA) to galvanized (GI) transition, when high Al content ingots are immersed in the bath. The flow, temperature, Al and Fe concentrations are solved for real operating conditions and the numerical results are compared with in-line measurements. Tests were performed at the Sorevco Inc. galvanizing line in Coteau-du-Lac, Québec. The Sorevco bath is smaller (75 ton) than the previously modelled bath (250 ton) but presented an ideal opportunity due to its location as well as its unique configurational and operational characteristics. Since the pot is small, variations in temperature and composition are more evident and more frequent. Also, the

DOI: 10.1002/fld

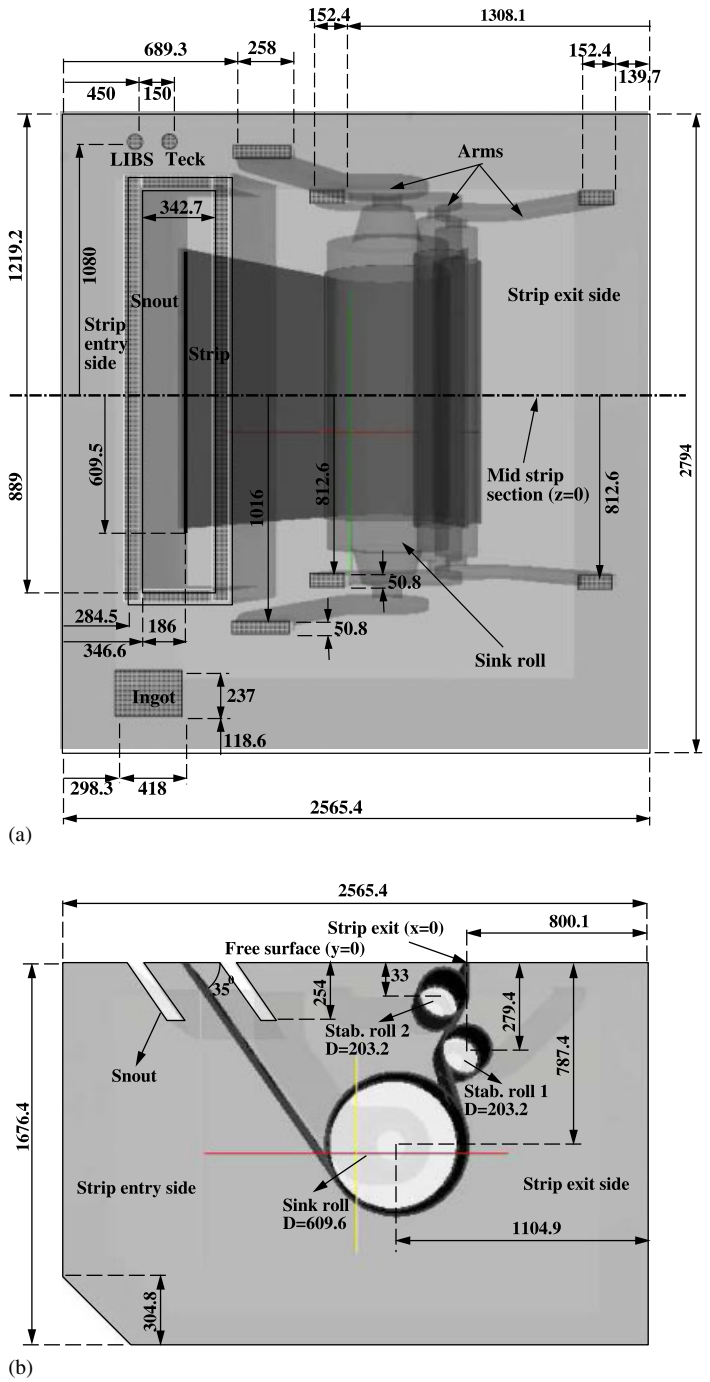

Figure 2. Geometry of the bath and probe location (dimensions are mm): (a) top view; and (b) front view.

DOI: 10.1002/fld

bath hardware is asymmetric due to side charging of ingots, and heat is supplied to the bath from electric resistance heaters (rather than inductors) as well as from the strip which enters at about 25°C above the bath temperature. As a result, the numerical modelling presents a more interesting and more difficult case than the modelling of an '*isothermal*' bath where the strip enters at the bath temperature. The local and temporal variations in flow, temperature and composition are thus more pronounced.

2. MATHEMATICAL MODEL

The numerical solution considers a full scale model of the bath geometry, including all hardware immersed in the bath (sink and stabilizer rolls, roll support arms, snout), the strip traversing the bath, heating of the bath and the effect of ingot melting. The bath model is based on the following assumptions:

(a) The liquid metal is incompressible;
(b) The flow in the bath is turbulent;
(c) Buoyancy effects are considered using the Boussinesq approximation;
(d) Time-dependent effects are important and, therefore, are considered in the simulation;
(e) The liquid Zn–Al alloy behaves as a Newtonian fluid;
(f) The bath configuration is non-symmetrical; hence, the complete bath is modelled;
(g) The level of the liquid in the bath is considered constant such that the removal of melt as coating on the strip and the addition of material from the ingot compensate each other in time;
(h) Ingot immersion is gradual, hence we neglect the geometrical change caused by the ingot presence and consider only the thermal and compositional effect of the ingot melting;
(i) Solubility limits of Al and Fe in the solution are taken from the data of Tang [17].

The flow of liquid zinc in the bath is described by the incompressible Reynolds-averaged Navier–Stokes equations

$$\rho\left(\frac{\partial \mathbf{u}}{\partial t}+\mathbf{u}\cdot\nabla\mathbf{u}\right)=-\nabla p+\nabla\cdot[2(\mu+\mu_T)\dot{\gamma}(\mathbf{u})]-\rho\mathbf{g}\beta_T(T-T_0)-\rho\mathbf{g}\beta_{\mathrm{Al}}(c_{\mathrm{Al}}-c_{\mathrm{Al}_0}) \tag{1}$$

$$\nabla\cdot\mathbf{u}=0 \tag{2}$$

where $\dot{\gamma}(\mathbf{u})=(\nabla\mathbf{u}+(\nabla\mathbf{u})^{\mathrm{T}})/2$ is the strain rate tensor. The heat transfer is modelled by the energy equation

$$\rho c_p\left(\frac{\partial T}{\partial t}+\mathbf{u}\cdot\nabla T\right)=\nabla\cdot[(\lambda+\lambda_T)\nabla T]+Q_T \tag{3}$$

In the above equations t, $\mathbf{u}$, p, T, μ, c_p and λ denote time, velocity, pressure, temperature, viscosity, specific heat and thermal conductivity, respectively. The buoyancy term in the momentum equation, as given by the Boussinesq approximation, depends on the reference density (the density estimated at the reference temperature T_0 and Al concentration c_{Al_0}), gravity vector $\mathbf{g}$, thermal expansion coefficients β_T and β_{Al}, and the temperature and Al concentration difference between the liquid zinc and the reference values T_0 and c_{Al_0}, respectively. The source term Q_T in the energy equation models the heat lost during ingot melting.

DOI: 10.1002/fld

Aluminium and iron concentrations c_i (c_{Al} for the aluminium concentration and c_{Fe} for the iron concentration) are obtained by solving the mass transport equations

$$\rho\left(\frac{\partial c_i}{\partial t}+\mathbf{u}\cdot\nabla c_i\right)=\nabla\cdot[(D+D_T)\nabla c_i]+Q_i \tag{4}$$

where D is the molecular diffusion coefficient, D_T is the turbulent diffusion and Q_i is a volumetric source term used to model the effect of ingot additions.

2.1. Turbulence modelling

The turbulent viscosity μ_T and turbulent thermal conductivity λ_T are computed using the two-equation k–ε model of Launder and Spalding [18]. Two additional equations are solved, that of the turbulence kinetic energy k and turbulence dissipation ε

$$\rho\left(\frac{\partial k}{\partial t}+\mathbf{u}\cdot\nabla k\right)=\nabla\cdot\left[\left(\mu+\frac{\mu_T}{\sigma_k}\right)\nabla k\right]+P+G-\rho\varepsilon \tag{5}$$

$$\rho\left(\frac{\partial \varepsilon}{\partial t}+\mathbf{u}\cdot\nabla \varepsilon\right)=\nabla\cdot\left[\left(\mu+\frac{\mu_T}{\sigma_\varepsilon}\right)\nabla \varepsilon\right]+C_{\varepsilon 1}\frac{\varepsilon}{k}(P+G)-C_{\varepsilon 2}\rho\frac{\varepsilon^2}{k} \tag{6}$$

where P is the shear production term defined by

$$P=\mu_T[\nabla\mathbf{u}:(\nabla\mathbf{u}+\nabla\mathbf{u}^{\mathrm{T}})] \tag{7}$$

and G accounts for the effect of the buoyancy on the production of turbulence

$$G=\frac{\mu_T}{Pr_T}\beta\mathbf{g}\cdot\nabla T \tag{8}$$

Model constants σ_k, σ_ε, $C_{\varepsilon 1}$, $C_{\varepsilon 2}$, C_μ take on the standard values [18], $\sigma_k=1.0$, $\sigma_\varepsilon=1.3$, $C_{\varepsilon 1}=1.44$, $C_{\varepsilon 2}=1.92$, $C_\mu=0.09$.

The eddy viscosity, thermal conductivity and mass diffusion are computed from k and ε by

$$\mu_T=\rho C_\mu\frac{k^2}{\varepsilon} \tag{9}$$

$$\lambda_T=\frac{\mu_T c_p}{Pr_T} \tag{10}$$

$$D_T=\frac{\mu_T}{Sc_T} \tag{11}$$

with the turbulent Prandtl number Pr_T and the turbulent Schmidt number Sc_T equal to unity.

Turbulence equations are solved for the logarithms of turbulence variables [19, 20]. This change of dependent variables guarantees that k and ε will remain positive throughout the computations. Hence the eddy viscosity μ_T and the eddy conductivity λ_T will always remain positive. Moreover, solutions from logarithms are more accurate because the fields of the logarithmic variables present smoother variations than those of k and ε [19].

DOI: 10.1002/fld

2.2. Initial conditions

Initial conditions are considered for all variables, namely for velocity, pressure, temperature, turbulence variables and the Al and Fe concentrations. Flow variables ($\mathbf{u}$, p) correspond to a no flow condition. The initial TKE level k_i corresponds to a 1% turbulence based on a reference velocity of $u_{\text{ref}} = 1$ m/s

$$k_i = 0.01 u_{\text{ref}}^2 \tag{12}$$

and the initial TKE dissipation is computed from a one-equation turbulence model as

$$\varepsilon_i = \frac{C_\mu^{3/4} k_i^{3/2}}{l_m} \tag{13}$$

where $l_m = \kappa d$ is the mixing length, with κ being the Von Karman constant, $\kappa = 0.4$, and d the distance to the nearest wall. The initial temperature and bath composition are considered uniform and equal to the measured values at the time when the simulation starts: $T_i = 467.6°\text{C}$, $c_{\text{Al}_i} = 0.134$, $c_{\text{Fe}_i} = 0.044$ (concentrations are given in %wt).

2.3. Boundary conditions

In order to complete the mathematical definition of the problem, boundary conditions are also imposed for velocity, temperature, turbulence variables and Al and Fe concentrations. The free surface exposed to ambient air has a zero normal velocity and zero tangent shear stress condition. On the solid walls, a combination of Neumann (tangential) and Dirichlet (normal) conditions are imposed using wall functions

$$\left.\begin{aligned} [2(\mu + \mu_T)\dot{\boldsymbol{\gamma}}(\mathbf{u}) \cdot \mathbf{n} - p\mathbf{n}] \cdot \hat{\mathbf{t}}_i = \boldsymbol{\tau}_{\text{w}} \cdot \hat{\mathbf{t}}_i \\ \mathbf{u} \cdot \mathbf{n} = 0 \end{aligned}\right\} \quad \text{on } \Gamma_{\text{wall}} \tag{14}$$

The shear stress $\boldsymbol{\tau}_{\text{w}}$ prescribed by the wall function is imposed on the tangential directions $\hat{\mathbf{t}}_i$ defining the tangent plane, while the normal velocity is constrained to be zero. The tangency condition is imposed in a nodal fashion (see [6] for more details).

The TKE values at boundary points k_{w} are computed implicitly by setting the normal derivative of the TKE to zero at the wall, while the TKE dissipation rate on boundary points is obtained by using

$$\varepsilon_{\text{w}} = \frac{C_\mu^{3/4} k_{\text{w}}^{3/2}}{\kappa y} \tag{15}$$

Free boundary conditions (zero normal derivative) are imposed on the free surface for both k and ε.

For temperature boundary conditions, a temperature wall function is required on solid walls [21]. The procedure is similar to that used for the velocity and consists of imposing a wall heat flux given by

$$q_{\text{w}} = h_T (T - T_{\text{w}}) \tag{16}$$

$$h_T = \frac{\rho c_p C_\mu^{1/4} k_{\text{w}}^{1/2}}{T^+} \tag{17}$$

DOI: 10.1002/fld

where T_w is the wall temperature and T^+ is function of y^+ (see [21] for more details). At the bath walls, in addition to the temperature wall function, the boundary conditions take into account the heat loss through walls. This is modelled using a convective heat flux

$$q_w = h_c(T_w - T_a) \tag{18}$$

where h_c is a heat transfer coefficient and T_a is the ambient temperature. The wall function coupled with the convection heat transfer through walls results in a wall heat flux given by

$$q_w = h(T - T_a) \tag{19}$$

in which h is an equivalent heat transfer coefficient, $h = h_T h_c/(h_T + h_c)$. The heating of the walls starts when the bath temperature drops under 466.5°C and the heating is turned off when the temperature reaches 467.5°C. During the heating period the temperature outside the bath walls is 550°C and decreases down to 480°C during the no heating periods at a rate of 3.5°C/ min. The heat transfer coefficient at the bath walls is considered $h_c = 100\,\mathrm{W/(m^2\,°C)}$. The heat lost through radiation at the top surface was estimated to be one order of magnitude lower than the heat lost by convection and hence it was neglected in this work. The ambient temperature is considered $T_a = 30$°C. The surface of the bath is covered by a layer of mushy dross except for a region around the strip exit where the air flow from the air knifes exposes the liquid zinc to the ambient air. Since, the heat transfer coefficient is considered to be $h_c = 20\,\mathrm{W/(m^2\,°C)}$ on the dross covered part of the top surface and $h_c = 200\,\mathrm{W/(m^2\,°C)}$ around the strip exit.

For the Al and Fe we consider that there is no mass flux at the bath walls and free surface. The boundary conditions at the strip surface and those modelling the ingot presence are discussed hereafter.

2.4. Modelling of the ingot melting and surface strip reaction

The melting of the ingots is modelled using source terms in the temperature and concentration equations. For example, the source term in Equation (4) representing the mean Al mass rate in the ingot melting volume is given by

$$Q_{Al} = \frac{M_{ingot}(c_{ingot} - c_{bath})}{V_{ingot}\Delta t} \tag{20}$$

where $M_{ingot} = 1000$ kg is the ingot mass, $V_{ingot} = 0.119\ \mathrm{m^3}$ is the volume of the region where the melting take place, c_{ingot} is the Al concentration of the ingot (1% for the white ingots and 4.5% for the blue ingot), c_{bath} is the Al concentration in the bath and Δt is the actual melting time ($\Delta t = 10$ min for the white ingots and $\Delta t = 16$ min for the blue ingot).

A similar source term is imposed in the Fe concentration equation. Since the ingots have no Fe, we consider $c_{ingot} = 0$ and c_{bath} takes on the Fe concentration in the bath.

Aluminium consumption on the strip surface is assumed to take place on the first 0.305 m of the strip length from his entry on the bath (corresponding to 0.2 s at a trip velocity of 1.524 m/s). The overall Al concentration of the coating is considered to be 0.4% by weight for a coating weight of $0.2\,\mathrm{kg/m^2}$ per side. The mean Al consumption flux is given by

$$(q_{Al})_{strip} = -\frac{0.2\,\mathrm{kg/m^2}}{0.305\,\mathrm{m}} V_{strip}(c_{Al})_{strip} \tag{21}$$

DOI: 10.1002/fld

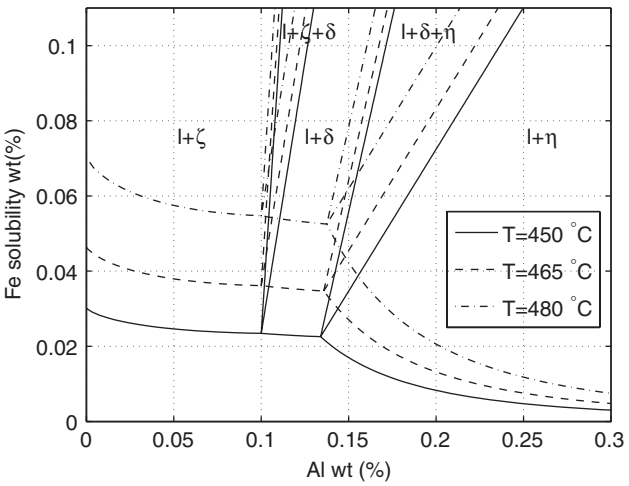

Figure 3. Solubility limit of Fe and Al in the Zn–Al–Fe alloys.

The Al mass flux on the strip surface near the entry in the bath is therefore $(q_{\mathrm{Al}})_{\mathrm{strip}} = -0.4\ \mathrm{kg}/(\mathrm{m}^2\mathrm{s})$. This term is considered through the Neumann boundary condition in the finite element formulation.

2.5. Solubility limit in the Zn rich corner of the Zn–Al–Fe alloys

The solubility limit of iron in molten Zn–Al alloys depends on the temperature and was determined experimentally by Tang [17]. For small contents of Al in the Zn–Al–Fe alloy, the intermetallic compound in equilibrium with the liquid changes from the ζ ($FeZn_{13}$) to δ ($FeZn_7$) and then to the η (Fe_2Al_5) phase for increasing Al concentrations (see Figure 3). The first two intermetallic compounds all contain some Al in solid solution and the η phase, whereas the η phase contains Zn in solid solution [22].

The Fe solubility in liquid Zn (no Al in solution) satisfies the equation

$$c^0_{\mathrm{Fe}} = \exp\left(17.78 - \frac{15\,388}{T}\right) \tag{22}$$

where T is the temperature expressed in K. The solubility limit of Fe in Zn–Al alloys is then determined as follows:

- phase ζ:

$$\begin{gathered} c_{\mathrm{Fe}} = c^0_{\mathrm{Fe}} \exp[14(4.1 c_\zeta c^0_{\mathrm{Al}} + c_\zeta \ln(c_\zeta) + c^0_{\mathrm{Al}} \ln(c^0_{\mathrm{Al}}))/c_\zeta] \\ \text{with } c^0_{\mathrm{Al}} = 0.164 c_{\mathrm{Al}} \quad \text{and } c_\zeta = 1 - c^0_{\mathrm{Al}} \end{gathered} \tag{23}$$

- phase δ:

$$\begin{gathered} c_{\mathrm{Fe}} = 1.22 c^0_{\mathrm{Fe}} \exp[8(3 c_\delta c^0_{\mathrm{Al}} + c_\delta \ln(c_\delta) + c^0_{\mathrm{Al}} \ln(c^0_{\mathrm{Al}}))/c_\delta] \\ \text{with } c^0_{\mathrm{Al}} = 0.42 c_{\mathrm{Al}} \quad \text{and} \quad c_\delta = 1 - c^0_{\mathrm{Al}} \end{gathered} \tag{24}$$

Table I. Configuration studied.

Strip entry angle	Snout depth	Strip width	Roller depth	Bath height	Bath temperature	Strip temperature	Strip velocity
35°	0.254 m	1.219 m	0.787 m	1.676 m	467.6°C	495°C	1.524 m/s

- phase η:

$$c_{\mathrm{Fe}}^2 c_{\mathrm{Al}}^5 = \exp\left(28.1 - \frac{33\,066}{T}\right) \tag{25}$$

where c_{Al} is the saturated Al in solution.

The ζ phase forms when the Al content in solution is less than 0.1%, the phase δ precipitates for Al contents between 0.1% and c_{Al}^* (c_{Al}^* being at the intersection of the two curves described by Equations (24) and (25) known as the 'knee point'), whereas the phase η precipitates for Al contents higher than c_{Al}^*. Therefore, any excess aluminium and iron will be present in form of precipitates of Fe_2Al_5 (top dross) for bath Al contents above c_{Al}^* and in the form of ζ and δ particles (bottom dross) for Al levels lower than c_{Al}^*. Figure 3 shows the phase diagram at 450, 465 and 480°C.

3. FINITE ELEMENT SOLUTION

The global system of equations is solved in a partly segregated manner [6]. The solution algorithm is illustrated in Figure 4. At each time step global iterations are performed for the momentum-continuity, turbulence, energy and composition equations. Sub-iterations of turbulence transport equations are also used to accelerate the overall convergence of the iterative process. In the initial solution there is no flow and the temperature and compositional distribution are uniform.

The Navier–Stokes and scalar transport equations are solved using a streamline-upwind Petrov–Galerkin (SUPG) method [23, 24]. This method contains additional stabilization terms providing smooth solutions to convection dominating flows. The SUPG method also deals with velocity–pressure coupling so that equal-order interpolation results in a stable numerical scheme. This allows the use of simple linear elements for all variables.

4. APPLICATION

4.1. Bath configuration

Table I summarizes the main geometrical and operational parameters for the specific Sorevco bath configuration. The bath is 2.57 m long, 2.79 m wide and 1.68 m deep. A three-hour period of the GA–GI transition was chosen for the numerical simulation covering a continuous operation (no line shut down) and where three jumbo ingots (1 ton) were charged into the bath. This period represents the largest variation in bath Al composition and temperature fluctuation.

DOI: 10.1002/fld

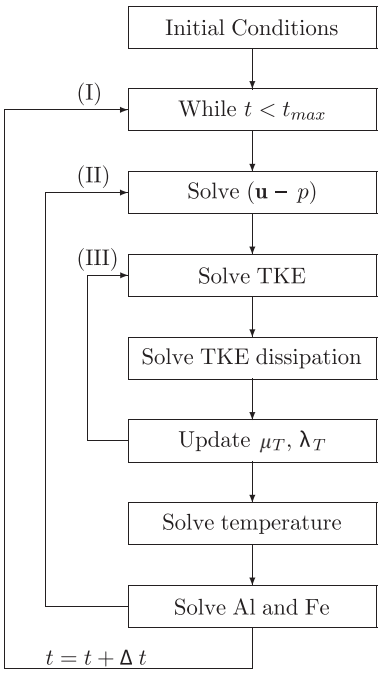

Figure 4. Solution algorithm.

Constant material properties were used for the calculations using the data for Zn + 0.14%Al at 460°C: density $\rho = 6600\ \mathrm{kg/m^3}$; laminar viscosity $\mu = 0.004$ Pa s; specific heat $c_p = 512\ \mathrm{J/kg\,K}$; thermal conductivity $\lambda = 60\ \mathrm{W/m\,K}$; thermal expansion coefficient $\beta_T = 1.38 \times 10^{-4}\ \mathrm{K^{-1}}$; Al concentration expansion coefficient $\beta_{\mathrm{Al}} = 0.0166$.

The computational domain was discretized using four-node tetrahedral elements with a mesh of 143 331 nodes and 795 807 elements. Computations were performed in parallel on a Beowulf cluster composed of Pentium III processors running at 1 GHz, connected by a 100-Mbps Fast Ethernet network. The time step of the transient solution is 6 s, resulting in a total of 1800 solutions covering the three-hour period of simulation. The computational time for a complete run is about 7 days when using 32 processors.

4.2. Numerical results

Transient state computations were carried out starting at 10h45 (corresponding to 645 min) for a period of 180 min covering three ingot additions. The first ingot was white (1% Al, melting begins at $t = 646$ min), followed by the immersion of a blue ingot (4.5%Al) at $t = 711$ min and a second white ingot at $t = 789$ min. Two simulations were carried out: first, the solution is obtained by neglecting the density dependence upon the Al concentration ($\beta_{\mathrm{Al}} = 0$) identified hereafter as

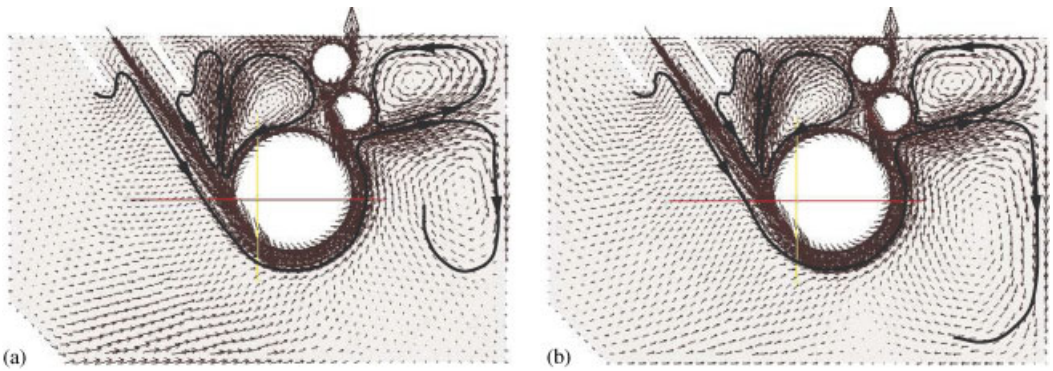

Figure 5. Velocity distribution through the strip mid-plane ($z = 0$) during blue ingot melting ($t = 719$ min): (a) solution $S1$; and (b) solution $S2$.

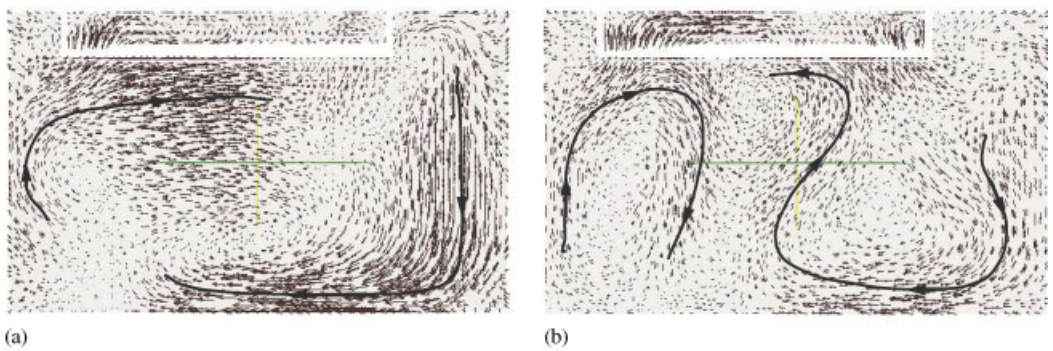

Figure 6. Velocity distribution in a plane parallel to the strip ($x = -1300$) during blue ingot melting ($t = 719$ min): (a) solution $S1$; and (b) solution $S2$.

$S1$ and then a second run was made taking into account for the buoyancy effect caused by the non-uniform Al distribution ($S2$).

The velocity distribution during the blue ingot melting ($t = 719$ min) is shown in Figures 5 and 6. The solution on the left-hand side is for the condition $S1$, whereas on the right is shown the solution $S2$. Figure 5 illustrates the velocity in a plane parallel with the direction of the strip movement passing through the strip mid-plane. As can be seen the solutions are similar indicating that the velocity in this plane is mostly determined by the strip movement and less affected by buoyancy. Larger differences are observed in Figure 6 showing the velocity in a plane parallel to the snout and strip entry. This section crosses also the ingot melting volume which is located on the upper right corner. The solution $S1$ indicates that, when considering only the temperature in the buoyancy term, the lower temperature liquid metal from the ingot melting region flows rapidly towards the bottom of the bath. Liquid zinc from the other side of the bath (left side in Figure 6) flows upwards and then across the bath to fill the space left by the cold metal from the

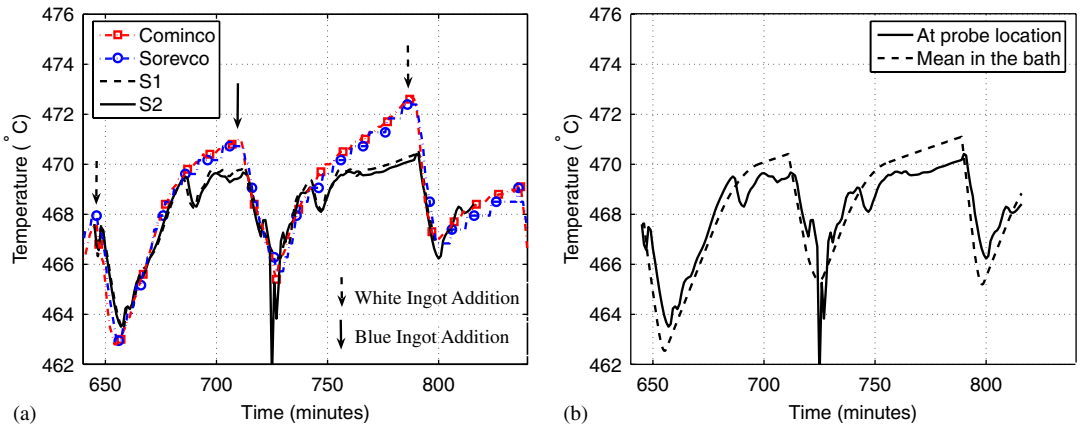

Figure 7. Evolution in time of the temperature: (a) mean simulated temperature; and (b) temperature at probe location ($S2$).

ingot. The flow pattern is dramatically changed when considering the Al buoyancy. The liquid from the melting region does not go downward. Instead, smaller metal currents are formed, one at the bottom of the bath in the right-hand side and another with an inverse U shape on the left side of the bath.

The temperature evolution in time is shown in Figure 7. In Figure 7(a), the temperature measured by the Teck Cominco and Sorevco thermocouples is compared with the computed temperature at the probe location. The temperature decreases during ingot melting periods and increases during the interval between two ingot meltings as a result of the bath wall heating and of the strip entering at a higher temperature. The computed temperature is in good agreement with the measured values during the ingot melting period and during the first part of the interval between two ingot melting periods. This indicates that the numerical model accounts correctly for the effect of ingot melting and bath heating from the wall heaters and from the strip. Note that the results from simulations $S1$ and $S2$ are similar except during the blue ingot melting. When the effect of Al on the density is neglected (simulation $S1$) the metal from the ingot has lower temperature and hence higher density, flowing towards the bottom of the bath. However, as the Al concentration in the ingot is 4.5%, much higher than the Al content in the bath, the simulation $S2$ shows that the Al rich metal will have lower density and tend to flow towards the top of the bath. This explains the lower temperature during the blue ingot melting observed in simulation $S2$ at the probe location, which is close to the top of the bath. Figure 7(b) shows the comparison between the mean temperature in the bath and the temperature computed at the probe location for simulation $S2$. The temperature at the probe is higher during and after the ingot melting and is lower than the mean temperature during the periods before ingot immersion. During the periods before ingot immersion the computed temperature at probe location is lower than both measured values and the mean bath temperature. This is caused by the flow of liquid zinc with lower temperature from the top strip exit side of the bath towards the side where the probe is located. The material around the strip exit is at lower temperature as is cooled by the air knives. The difference between the computed and measured temperature may then be explained by an overestimation of the cooling from air knives.

DOI: 10.1002/fld

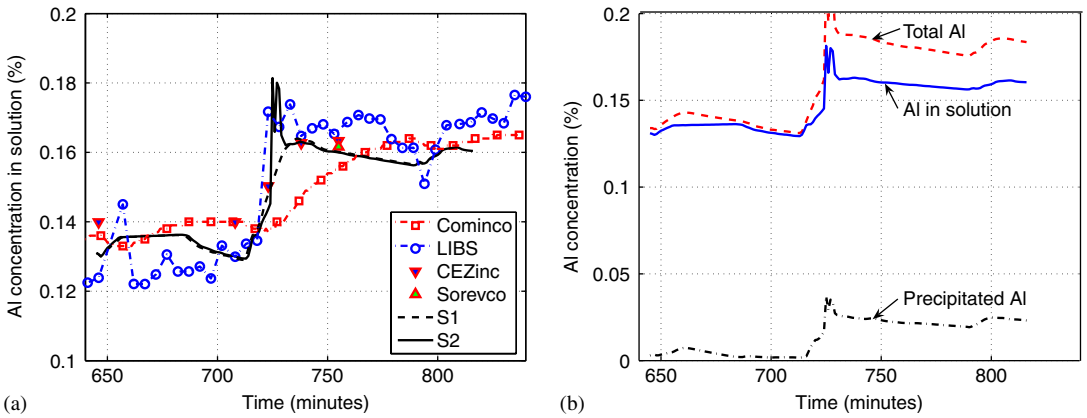

Figure 8. Evolution in time of the Al concentration at probe location: (a) measured and computed Al in solution; and (b) total, in solution and precipitated Al (*S*2).

The coupled mass and heat transfer solutions have resulted in a clear and consistent representation of the distribution of Al in the bath for the simulated cycles of an ingot melting period followed by a period with no ingot in the bath. As the ingot melts, the local total Al content increases according to the temperature and motion induced flows. During this initial period, the total Al represents the amount in solution and the amount that is in precipitated form. Assuming that the precipitated Al is very finely dispersed, it will be displaced at the same speed as the liquid Zn in the bath. When these particles are transported into the region of higher temperature, they are assumed to dissolve instantly according to the solubility limits given by Tang [17]. In Figure 8(a), the computed effective Al concentration at the probe location is compared with the concentrations measured by the Teck Cominco Al sensor and by the LIBS system, and with the bath analytical results [25]. The LIBS data points were averaged over five minute intervals. The bath sample analyses are reported as dissolved Al based on a Noranda software that calculates this value from the total Al content. The results indicate that the numerical solution is in excellent agreement with the LIBS measurements. The data obtained by Teck Cominco seems to react more slowly to changes in the bath content and the values indicated are more averaged in time. As can be seen in Figure 8(a), the numerical model is able to predict the decrease in the Al content in solution during the periods without ingot melting and the increase in the Al content in solution during ingot melting. The magnitude of the Al concentration change during the blue ingot melting was also well predicted by the numerical model. The results show that, as observed for the determination of temperature variations, the simulations *S*1 and *S*2 produce similar results, except for a short period of time during the melting of the ingot with higher Al content. This indicates that the buoyancy determined by the non-uniform Al distribution is significant only when large Al concentration gradients are present in the bath. As soon as the Al distribution becomes more uniform the density dependence on the Al content has almost no influence on the flow. Figure 8(b) shows the computed value for the total Al, Al in solution and the precipitated Al at the probe location for the simulation *S*2. Precipitates are formed during ingot melting because of the combined effects of an increase in Al and a decrease in temperature. At the start of the simulation period, the initial Al concentration at 0.134% corresponds to precipitates in the form of bottom dross. Hence the dross particles

DOI: 10.1002/fld

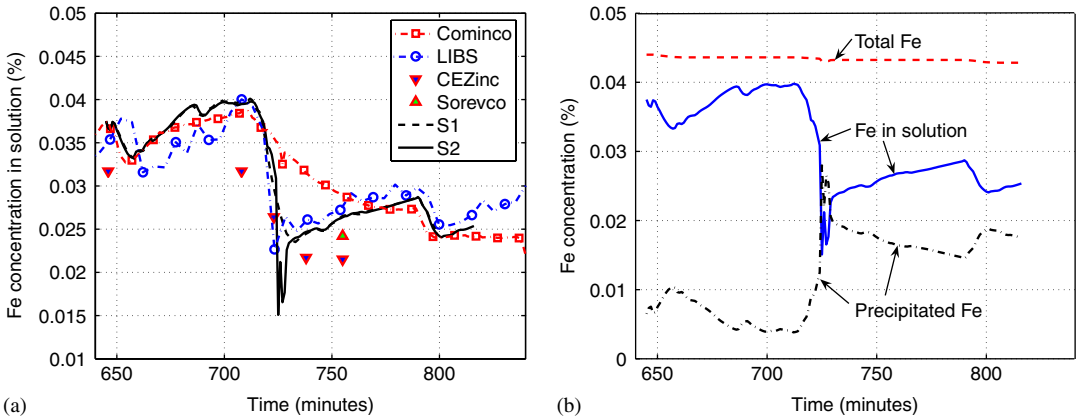

Figure 9. Evolution in time of the Fe concentration at probe location: (a) measured and computed Fe in solution; and (b) total, in solution and precipitated Fe (*S*2).

circulating with the flow contains only small amounts of Al. During the simulation, the Al content increases and some of the precipitated Fe converts to Fe_2Al_5 top dross.

Computations for the Fe concentration take into account the melting of ingots with no Fe content. The rates of dissolution of Fe from the strip and from the bath hardware was neglected since these are very small amounts compared to the Fe content in the bath. In Figure 9(a), the computed Fe concentration at the probe location is compared with the concentration determined by Teck Cominco from the measured temperature and Al content and the values measured by LIBS. Bath analytical results from the samples analysed by CEZinc and Sorevco are also shown. The results indicate again that the numerical solution is in excellent agreement with the LIBS measurements and with the Teck Cominco values computed from the Al content. The numerical model correctly predicts the increase in the Fe content in solution during the periods without ingot melting (caused by the increase of the temperature and therefore an increase in the solubility limit) and the decrease in the Fe content in solution during ingot melting. The magnitude of the variations during the ingot melting periods were also well predicted by the numerical model.

Figure 9(b) shows the computed value at the probe location for the total Fe, Fe in solution and the precipitated Fe for simulation *S*2. Again, we can see that precipitates are formed during ingot melting ($t = 646$–656 min for the first white ingot, $t = 711$–727 min for the blue ingot, and $t = 789$–799 min for the second white ingot). The numerical model predicts the sharp decrease in the dissolved Fe when the blue ingot is immersed. This can be explained by the precipitation of particles of dross as a result of an increase in Al in the bath and a decrease in the temperature. During the blue ingot immersion, both Al in solution and precipitated Al concentrations were found to increase. The quantity of Fe in solution increases during the periods without ingot melting. This is caused by the dissolution of dross particles as a result of an increased temperature and a decrease in the total Al in the bath. During this time the Al concentration in solution decreases.

The local (probe location) and global variation in time of the total Al and Fe concentrations are compared in Figure 10. Differences between the local and bath mean values are important only during the ingot melting periods. During the periods of time when no ingot is melting the concentration of Al and Fe is quite uniform throughout the bath. Ingot immersion results

DOI: 10.1002/fld

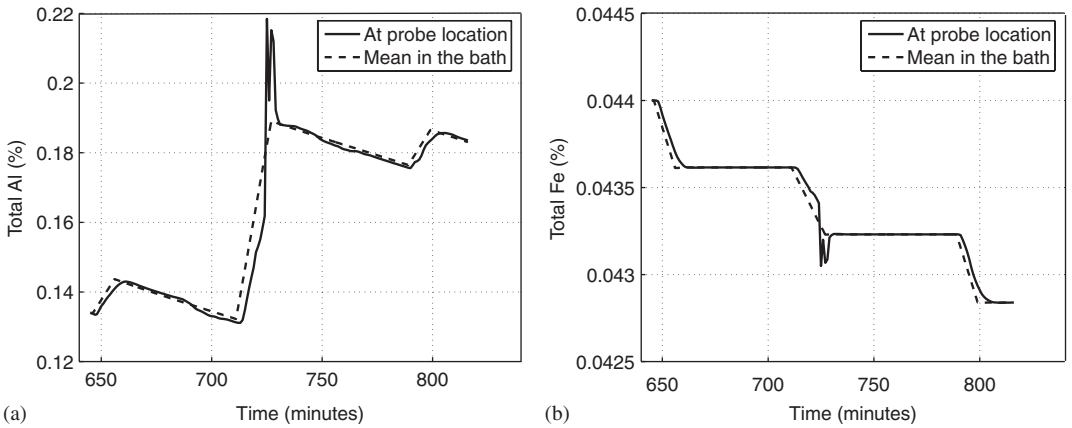

Figure 10. Al and Fe content at probe location compared with mean values (*S*2): (a) total Al; and (b) total Fe.

in a rapid increase in the Al content in the bath. The Al concentration at the probe location occurs approximately 3 min after the ingot immersion, data that is in agreement with previous experimental observations [2].

5. CONCLUSION

The following conclusions can be drawn from the numerical results obtained:

- The transient temperature evolution predicted by the numerical model agrees well with both series of measurements carried out by using the Teck Cominco sensor and the Sorevco instrumentation. This indicates that the numerical models for ingot melting, bath heating and bath cooling perform well. The observed discrepancies in the local temperature before ingot immersion indicate that the cooling determined by the air knifes was overestimated.
- The buoyancy effect determined by the non-uniform Al distribution is significant only when large Al concentration gradients are present in the bath (during the blue ingot melting).
- The calculated values for Al and Fe determined by the model agree very well with the experimental values using LIBS monitoring technique. The data obtained by Teck Cominco seem to react more slowly to changes in the bath content and the values indicated are more averaged in time.
- The numerical model predicts the sharp decrease in the Fe in solution when the blue ingot is immersed. This is explained by the precipitation of particles of dross as a result of a reported increase in Al in the bath and a decrease in the temperature. During the blue ingot immersion both Al in solution and precipitated Al concentrations were found to increase.
- At the start of the simulation period, the initial Al concentration at 0.134% corresponds to precipitates in the form of bottom dross. During the simulation, the Al content increases and some of the precipitated Fe converts to Fe_2Al_5 top dross.

DOI: 10.1002/fld

- The agreement between the numerical solution and experimental data confirms the assumption that the rate of nucleation and dissolution of dross particles is very rapid compared with the time scale which represents the changes caused by the ingot melting and Al uptake on the strip and can thus be considered almost instantaneous.

ACKNOWLEDGEMENTS

The authors would like to acknowledge the International Lead Zinc Research Organization (ILZRO) and the industrial sponsors for funding this project. The authors also wish to acknowledge M. Sabsabi, L. St. Onge, R. Héon from IMI and T. A. E. Cormode, N. Y. Tang from Teck Cominco for the experimental data and the contribution of Michel Perrault in creating the bath mesh for the simulation.

REFERENCES

1. Ajersch F, Gauthier M, Binet C. Kinetics of continuous galvanizing process. In *Fundamentals of Metallurgical Processing—J. M. Toguri Symposium*, Kaiura G, Pickles C, Utigard T, Vahed A (eds), 2000; 161–178.
2. Paré A, Binet C, Ajersch F. Numerical simulation of 3-D flow in a continuous strip galvanizing bath. *GALVATECH'95*, Iron & Steel Society, 1995; 695–706.
3. Ajersch F, Binet C, Goodwin FE, Turke KS, Kolisnyk PS. Validation studies of the numerical simulation of flow in the Bethlehem Steel, Burns Harbor galvanizing bath. *GALVATECH'98*, Iron & Steel Society, 1998; 642–647.
4. Gagné M, Gang M. Numerical modeling of fluid flow pattern in a continuous galvanizing bath. *GALVATECH'98*, Iron & Steel Society, 1998; 90–95.
5. Otsuka K, Arai M, Kasai S. Development of dross control methods in a continuous galvanizing pot by numerical bath flow analysis. *GALVATECH'98*, Iron & Steel Society, 1998; 96–101.
6. Ilinca F, Hétu J-F, Ajersch F. Three-dimensional numerical simulation of turbulent flow and heat transfer in a continuous galvanizing bath. *Numerical Heat Transfer*, *Part A* 2003; **44**:463–482.
7. Ajersch F, Ilinca F, Hétu J-F. Simulation of flow in a continuous galvanizing bath: Part I. Thermal effects of ingot addition. *Metallurgical and Materials Transactions B* 2004; **35**:161–170.
8. Ajersch F, Ilinca F, Hétu J-F. Simulation of flow in a continuous galvanizing bath: Part II. Transient aluminum distribution resulting form ingot addition. *Metallurgical and Materials Transactions B* 2004; **35**:171–178.
9. Ajersch F, Trépanier L, Goodwin FE. Particle size and composition of dross particles from galvanize and galvanneal operations. *44th MWSP Conference Proceedings*, Iron & Steel Society, 2002; 771–780.
10. Liu YH, Tang N-Y, Zhang L, Denner SG, Goodwin FE. Dross formation and control during transition from galvannealing to galvanizing. *44th MWSP Conference Proceedings*, Iron & Steel Society, 2002; 781–790.
11. Ouellet L, Ajersch F, Ilinca F. Numerical simulation and validation of flow in a galvanizing bath using a water model. *GALVATECH'04*, Iron & Steel Society, 2004; 917–926.
12. Ilinca F, Hétu J-F, Ajersch F. Numerical simulation of Al and Fe distribution during continuous galvanizing operations. *GALVATECH'04*, Iron & Steel Society, 2004; 1067–1078.
13. Ajersch F, Ilinca F, Hétu J-F, Goodwin FE. Numerical simulation of the rate of dross formation in continuous galvanizing baths. *AISTech'05*, Association for Iron & Steel Technology, 2005.
14. Tang NY. Refined 450°C isotherm of Zn–Fe–Al phase diagram. *Materials Science and Technology* 1995; **11**:870–873.
15. Gagné M, Baril A, St-Onge L, Sabsabi M, Lucas J-M. On-line chemical analysis of CGL baths using laser induced breakdown spectroscopy. *Galvanizers Association 96th Meeting*, 2004.
16. Liu YH, Cormode TAE, Filc AB, Tang NY. Development of the Teck Cominco new generation G2 aluminum sensor. *Galvanizers Association 96th Meeting*, 2004.
17. Tang N-Y. Determination of liquid-phase boundaries in Zn–Fe–Mx Systems. *Journal of Phase Equilibria* 2000; **21**(1):70–77.
18. Launder BE, Spalding DB. *Mathematical Models of Turbulence* (6th edn). Academic Press: London, 1972.
19. Ilinca F, Pelletier D. Positivity preservation and adaptive solution for the k–ε model of turbulence. *AIAA Journal* 1998; **36**(1):44–50.
20. Ilinca F, Pelletier D, Garon A. Positivity preserving formulations for adaptive solution of two-equation models of turbulence. *27th AIAA Fluid Dynamics Conference*, AIAA Paper 96-2056, 1996.

21. Ignat L, Pelletier D, Ilinca F. An adaptive finite element method for turbulent heat transfer. *34th AIAA Aerospace Sciences Meeting and Exhibit*, AIAA Paper 96-0607, 1996.
22. Tang N-Y. Characteristics of continuous galvanizing baths. *Metallurgical and Materials Transactions B* 1999; **30**:144–148.
23. Ilinca F, Hétu J-F. Finite element solution of three-dimensional turbulent flows applied to mould-filling problems. *International Journal for Numerical Methods in Fluids* 2000; **34**:729–750.
24. Franca LP, Frey SL. Stabilized finite element methods: II. The incompressible Navier–Stokes equations. *Computer Methods in Applied Mechanics and Engineering* 1992; **99**:209–233.
25. Ajersch F, Ilinca F, Sabsabi M, St-Onge L, Héon R, Cormode TAE, Tang N-Y, Baril C, Gagné M, Goodwin FE. Monitoring of Al and Fe content and numerical simulation of the Sorevco galvanizing bath during GA to GI transition. *Galvanizers Association 97th Meeting*, 2005.

DOI: 10.1002/fld